



SnO₂ nanotube arrays grown via an *in situ* template-etching strategy for effective and stable perovskite solar cells



Chaomin Gao^{a,1}, Shuai Yuan^{b,1}, Bingqiang Cao^{b,*}, Jinghua Yu^{a,*}

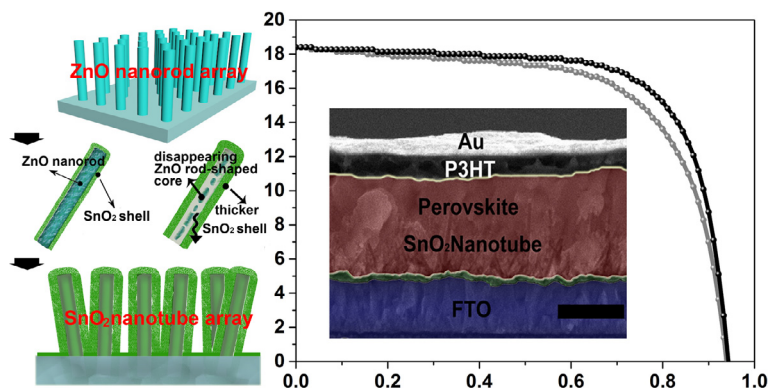
^aSchool of Chemistry and Chemical Engineering, Materials Research Center for Energy and Photoelectrochemical Conversion, University of Jinan, Jinan 250022, Shandong, China

^bSchool of Material Science and Engineering, Materials Research Center for Energy and Photoelectrochemical Conversion, University of Jinan, Jinan 250022, Shandong, China

HIGHLIGHTS

- A novel *in situ* template self-etching (iTSE) strategy is adopted to grow hollow domed SnO₂ nanotube array.
- The growth mechanism of such SnO₂ nanotubes is proposed based on a series of controllable experiments.
- Stable perovskite solar cells with SnO₂ nanotubes as effective ETL demonstrate high power conversion efficiency.

GRAPHICAL ABSTRACT



ARTICLE INFO

Article history:

Received 10 February 2017

Received in revised form 24 April 2017

Accepted 13 May 2017

Available online 15 May 2017

Keywords:

Perovskite solar cell

SnO₂ nanotube

Template-etching

Electron-transporting layer

ABSTRACT

For typical planar perovskite solar cell, an electron transporting layer (ETL) plays an important role in extracting electrons from a perovskite layer and blocking electron-hole recombination at the perovskite/conductive substrate interface. To date, TiO₂ or ZnO ETLs are mainly adopted in both forms of film and nanostructure due to their ease of preparation. Nevertheless, the photoinstability of TiO₂ and thermal instability of ZnO/perovskite interface remain the major challenges limiting their potential commercialization. Herein, we demonstrate an effective *in situ* template self-etching (iTSE) strategy to grow the novel hollow domed SnO₂ nanotubes array with ZnO nanorods as sacrifice templates and the growth mechanism of such SnO₂ nanotubes has been proposed based on a series of controllable experiments. Using such SnO₂ nanotube as ETL for perovskite solar cell demonstrates a high photocurrent density of 15.9 mA/cm² at a based-voltage of 760 mV, leading to a stable power conversion efficiency of 12.1% over 1000 s under the simulated AM 1.5G one sun illumination. This work highlights the importance of the ETL material selection and provides insights into achieving an ideal ETL/substrate homojunction to facilitate electron transporting.

© 2017 Elsevier B.V. All rights reserved.

1. Introduction

Organic-inorganic hybrid perovskites have been established as an important class of materials for photovoltaics, and unprecedented progress in increasing their power conversion efficiency (PCE) from 3.8% to 22.1% [1–12] was demonstrated in the past

* Corresponding authors.

E-mail addresses: mse_caobq@ujn.edu.cn (B. Cao), chm_yujh@ujn.edu.cn (J. Yu).

¹ These authors contributed equally.

few years. Such a rapid PCE increase is largely attributed to the continuous device structure developing, in which perovskite active layer is commonly sandwiched between a hole transporting layer (HTL) and electron transporting layer (ETL). Owing to the proper energy level matching and carriers transport property, photogenerated charge carriers are separated and extracted by ETL and HTL from perovskite film to external circuit with minimized energy loss [4]. Typically, such organic-inorganic hybrid perovskite solar cells (PSC) are of planar or mesoporous device structure depending on the morphology of ETL/HTL [5]. As a critical element of PSC, ETL plays a key role in achieving high-efficiency PSC benefiting from its function in setting up build-in electric field and selective transporting property for electrons. Actually, zinc oxide (ZnO) [8–10] and titanium dioxide (TiO₂) [11] are the most widely utilized ETL materials both in terms of dense film for planar device and nanostructure like nanoparticles or nanorods for mesoporous device. Although high efficiency solar cells were readily realized for both TiO₂ and ZnO, they still may exhibit some shortfalls. For example, the undoped TiO₂ ETL usually has relatively low electron mobility [13] but high processing temperature (100–450 °C). Moreover, TiO₂ is a typically great photocatalyst, which makes TiO₂ based cells less stable. Recently, Snaith et al. reported that perovskite solar cells using mesoporous TiO₂ are sensitive to ultraviolet (UV) illumination [14]. ZnO as a formidable competitor possesses a seemingly promising prospect. Nevertheless, any attempting to anneal the perovskite films grown on ZnO will lead to decomposition of the dark brown perovskite back into yellow PbI₂. Such apparent thermal instability of the perovskite/ZnO interface will undoubtedly have a deleterious effect on the long-term stability of the final devices and the physical reason is still under researching [15–18].

Tin dioxide (SnO₂), as an n-type semiconductor with a wide direct band gap of 3.6 eV at 300 K [19–21], is one of the promising multifunctional materials, which is more stable than TiO₂ under UV illumination [22,23]. Fluorine-doped SnO₂ (FTO) is already a robust transparent conducting electrode that has been widely utilized for PSC construction. Growing SnO₂ ETL on FTO substrate is a typical homogenous growth and will form an ETL/substrate interface with few defects, which is beneficial to electron transporting [24]. Previously, gelled SnO₂ nanoparticles have been used as ETLs for dye-sensitized solar cells (DSSC) [25]. In addition, Fang et al. first reported the low-temperature solution-processed SnO₂ film as an alternative ETL for planar perovskite solar cells with a PCE of 16%. They also improved the photovoltaic performance of such SnO₂-based planar perovskite solar cells by high-temperature magnesium doping [26,27]. Moreover, nanostructured SnO₂ is known to have higher electron mobility than nanostructured TiO₂ [23] and also a much more negative conduction band minimum (CBM) [28]. Exploitation of the low CBM of SnO₂ should facilitate increasing the open-circuit voltage of the PSC. Therefore, nanostructured SnO₂ is an interesting photoanode material, which could in principle facilitate efficient charge injection and charge collection. Although the photovoltaic conversion efficiency for cells employing SnO₂ are relatively poor in DSSC [25,29,30], it already shows great promise in PSCs [26,27,31]. For example, Murugadoss et al. [28] reported that a planar CH₃NH₃PbI₃ perovskite solar cell fabricated with SnO₂ film as ETL showing a PCE of 8.38%. However, to the best of our knowledge, SnO₂ nanotubes have not yet been reported for PSCs applications. One possible reason is the growth difficulty of one-dimensional (1D) and well-ordered SnO₂ nanorods or nanotubes on a given substrate for device fabrication. For example, till now, only a two-step nanowire template-assisted method was proved to be effective for SnO₂ nanotube growth, where the vapor phase growth of shell [32] and a second acid etching step [32,33] are necessary but either expensive or time-consuming. Synthesis of SnO₂ nanotube arrays on FTO glass sub-

strate for device applications with a simplified process still remains a challenge.

Herein, we proposed a simple but effective *in situ* template self-etching (*i*TSE) strategy to grow domed SnO₂ nanotube array (SnO₂-DNTs) with ZnO nanorods (NRs) as templates and demonstrated their successful application as effective and stable ETL for perovskite solar cell. A direct growth of SnO₂-DNTs based on the dissolving ZnO cores during the hydrothermal synthesis process of SnO₂ shell due to the *in situ* generated alkaline environment is achieved and the growth process is systematically investigated with a series of controlled hydrothermal experiments. Moreover, it provides a scenario for utilizing such SnO₂ nanostructure as an effective and stable ETL in perovskite solar cell. With the device configuration of glass/FTO/SnO₂-DNTs/perovskite/P3HT/Au, it is the first time to adopt SnO₂-DNTs scaffold layer to fabricate perovskite solar cell. Owing to its larger contacting area, prolonged incident optical length, and more effective photo carrier collecting ability, a stable PCE over 12% for such SnO₂ nanotube based solar cell is realized.

2. Experimental section

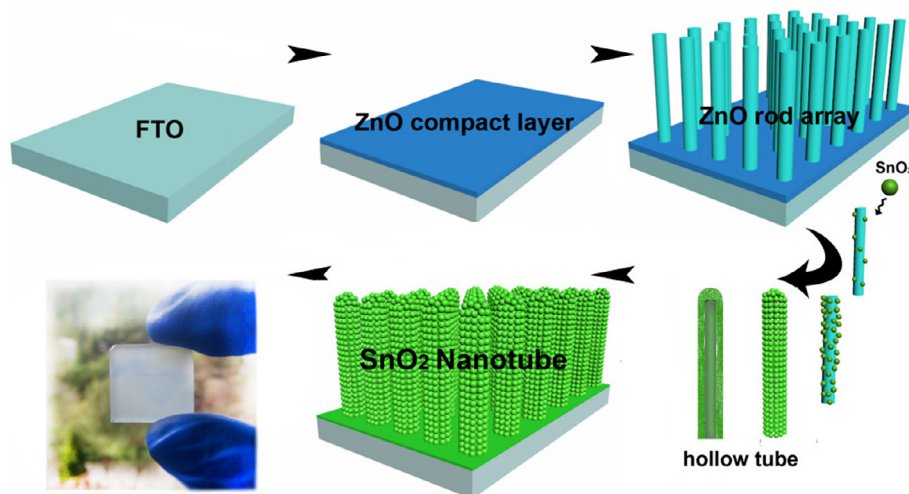
2.1. Synthesis of ZnO NRs and SnO₂-DNTs

First, a vertical array of ZnO NRs was grown on FTO/glass (sheet resistance ~15 Ω/square, 1.7 × 1.8 cm) substrate with a seeds-assisted approach, as we previously reported [34], which are utilized as the starting sacrifice templates. In addition, the dimensions of the substrates that used to fabricate the devices and the active area of the fabricated PSC are shown in Fig. S1. The preparation of SnO₂-DNTs was achieved with the *in situ* template self-etching (*i*TSE) strategy, as shown in Scheme 1.

Briefly, sodium stannate (6 mM) and urea (4 mM) were added into 15 mL of ethanol/water (60 vol% ethanol) mixed solvents, with magnetic stirring for about 10 min. Then the suspension was transferred to a 25 mL Teflon-lined stainless steel autoclave where the ZnO NRs grown on FTO/glass substrate was placed at an angle (~45°) against the wall of the autoclave, and heated in an electric oven at 170 °C for various time (15–90 min). With a hydrothermal reaction, the ZnO NRs are coated with a uniform nanostructured porous SnO₂ shell, which is constructed by tiny SnO₂ particles. Meanwhile, the ZnO NRs templates are *in situ* etched off by the self-generated alkali conditions with the reaction time prolonging, attributing to the hydrolyzation of urea. When the autoclave was cooled to room temperature, the substrate was rinsed with ultrapure water and allowed to dry at 60 °C in ambient air. A typical optical image of the SnO₂-DNTs grown on FTO substrate is presented in Scheme 1. This facile growth strategy provides a new way to prepare dense and uniform SnO₂-DNTs array with controllable wall thickness.

2.2. Perovskite solar cell fabrication and characterizations

Methylammonium iodide (MAI, 160 mg) and PbI₂ (461 mg) were dissolved in DMF at molar ratio of 1:1 to form the perovskite precursor solution. 30 μL of above solution was dropped onto the domed SnO₂ nanotube array (SnO₂-DNTs) coated substrate and spin-coated at 3000 rpm for 30 s, in which 150 μL chlorobenzene was dropped onto the center of spinning substrate after 8 s. Then the substrate was annealed at 100 °C for 1 h. P3HT solution was prepared by dissolving 20 mg P3HT in 1 mL chlorobenzene, and then 20 μL P3HT solution was spin-coated at 1000 rpm for 30 s to form the HTL. Finally, 50 nm Au electrodes were thermally evaporated at rate of 0.2 Å/s in vacuum. In addition, the PSCs employed ZnO NRs and TiO₂ NRs as ETLs were fabricated with the same pro-



Scheme 1. The schematic of preparation process. The SnO₂-DNTs were grown on FTO/glass substrates via a hydrothermal *in situ* template self-etching (iTSE) strategy with the as-prepared ZnO NRs as sacrifice templates.

tol. What's more, TiO₂ NRs were prepared with the hydrothermal method, as we previously reported [35]. The XRD measurements were carried out by using BRUKER-D8. The UV–visible (UV–vis) optical absorption spectrums were measured with a Shimadzu UV-3600 spectrophotometer and the incident light came from perovskite film side. The solar cell current density versus voltage (J–V) characteristics (from forward to reverse and from reverse to forward) were measured using a Keithley Source Meter 2612A under simulated AM 1.5G irradiation (100 mW/cm²) using a Xenon lamp based solar simulator (San-Ei, Class 3A, 150 W). Before measurements, the lamp was turned on for 15 min and the light intensity was calibrated using a NREL-traceable KG5 filtered silicon reference cell. The compliance was set at 3 mA, and the scanning step was 0.3 V/s without delay time. The maximum-power output stability of the solar cells was measured by monitoring the current density (J) output at the maximum-power voltage bias (obtained from the reverse J–V curves scan). The J-output is converted to PCE output using the following relation: $PCE = J(\text{mA}/\text{cm}^2) \times V(\text{V})/100(\text{mW}/\text{cm}^2)$. The incident photon to current conversion efficiency (IPCE) was measured using a QEX10 photoresponse system (PV Measurement). The wavelength interval was 10 nm and the intensity of the incident light from the monochromator was calibrated using a Si photodiode. The beam size of the incident light is smaller than devices area. The long-term stability of PSCs based on SnO₂-DNTs, TiO₂, and ZnO nanorods serving as ETL are carried out in glove box. In addition, the UV-irradiation stability of PSCs was also investigated with a UV lamp (267 nm, 16 W) in glove box. All the solar cells were directly tested without any encapsulation and the measurements were performed in ambient atmosphere.

3. Results and discussion

3.1. Characterizations of SnO₂-DNTs

Fig. 1(a–h) exhibit the representative plane and cross-sectional SEM images of ZnO NRs before and after the SnO₂ shell growth using sodium stannate and urea precursors with the different concentrations, while keeping the ratio of 1:9 and the reaction time of 60 min unchanged. Generally, the diameter of obtained products increases monotonously with the increasing precursor concentration in comparison with the pure ZnO NRs (Fig. 1a). However, almost no length change is observed (Fig. 1e–h). Actually, as shown

in Fig. 1(a and e), the as-prepared ZnO NRs with smooth surfaces vertically grow on the FTO/glass substrate and the diameter is approximately 40 nm (Fig. 1a inset) while the length is approximately 500 nm. After a hydrothermal reaction with the 2 mM precursor, the nanorods surfaces become rough with numerous tiny SnO₂ particulates as shown in Fig. 1(b and f). Such tiny SnO₂ particles construct the porous nanorod shell.

When the precursor concentration is increased to 6 mM, smoother SnO₂ shells with denser particles are observed, as seen in Fig. 1(c) and inset. However, from the corresponding SEM image of Fig. 1(g), we could clearly find that the ZnO NRs cores disappear, which means the obtained SnO₂ sample are dome-like hollow nanotubes rather than core-shell nanorods. The ZnO core NRs were *in situ* etched off during the SnO₂ nanotube formation. Compared with Fig. 1(a), the distinct increase of diameter of the obtained SnO₂-DNTs (Fig. 1d) was observed when the precursor concentration increased to 15 mM. As seen from Fig. 1(d and h), the excessive precursor continues to deposit on the SnO₂-DNTs, and it is difficult to distinguish the tubular structure.

The XRD patterns of the corresponding samples are shown in Fig. S2. The pure ZnO NRs present typical hexagonal wurtzite peaks of (100), (002), and (101). With the increasing concentration of stannate salt and urea, the intensity of the ZnO XRD peaks decrease and already disappear for the 6 mM sample. Meanwhile, the SnO₂ peaks at (110), (101), and (211) planes could be observed, which also confirms a gradual formation of SnO₂-DNTs and the etching process of ZnO NRs core. In addition, the optical absorption spectra of ZnO NRs and SnO₂-DNTs are measured and the bandgaps of ZnO nanorods and SnO₂-DNTs are indicated by the dashed lines, as shown in Fig. S3.

To further investigate the detailed microstructure of the obtained SnO₂-DNTs, transmission electron microscopy (TEM) characterization was carried out. TEM images exhibit clearly the dome-like morphology of SnO₂ nanotube with a diameter of about 100 nm and a shell thickness of about 30 nm, which is composed of SnO₂ nanoparticles as shown in Fig. 2(a and b), where the concentration of sodium stannate salt was fixed at 6 mM. Fig. 2(c) shows clearly that the SnO₂ tube wall is composed of nanoparticles. The lattice fringes of nanoparticle with a spacing of 0.34 nm corresponds to the (110) plane of rutile SnO₂. The TEM image and the corresponding FFT image (Fig. 2b, c and inset) also reveal that the SnO₂-DNTs have a typical polycrystalline structure in nature and O elements, respectively.

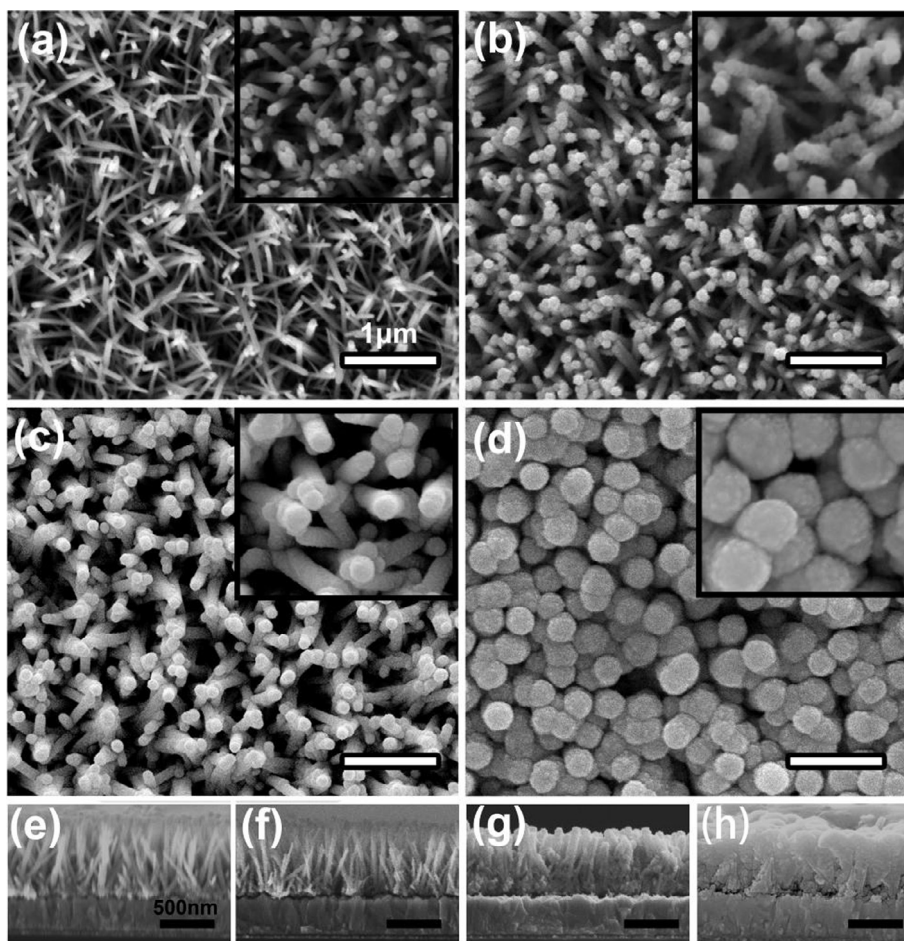


Fig. 1. The SEM images of ZnO NRs before and after SnO₂ shell coating with hydrothermal method. The SnO₂ precursors concentration are set at 0 mM (as-prepared ZnO NRs), 2 mM, 6 mM, and 15 mM, and the plane SEM images are shown in (a–d) and (e)–(h) present the corresponding cross-sectional SEM images, respectively.

To further confirm the composition of the SnO₂-DNTs, Fig. 3(a) displays an STEM image of a single sample collected with a high angle annular dark field detector (HAADF) attached to a TEM. The compositional line profiles (Fig. 3b) probed by energy-dispersive X-ray spectroscopy (EDS) show well-correlated Sn and O signals across the nanotube. Moreover, the signal intensity of Sn and O are stronger in the shell, which is further prove that the rod-shaped nanostructure is a hollow SnO₂ nanotube. To determine the surface chemical states of the resulting SnO₂-DNTs, X-ray photo-electron spectroscopy (XPS) spectra were measured. The high-resolution XPS spectra for Sn 3d (Fig. 3c) reveals the symmetric spin-orbital splitting of the Sn 3d_{5/2} and Sn 3d_{3/2} core level states of tin centered at 486.8 and 495.3 eV, respectively, which were assigned to the lattice tin oxide. The separation between the Sn 3d_{5/2} and Sn 3d_{3/2} level (8.5 eV) corresponds to the standard spectrum of Sn in SnO₂ reported in the literature [36,37]. The XPS peak at about 531.8 eV (Fig. 3b) corresponds to the O 1s state, which is the O²⁻ state in SnO₂.

3.2. Growth mechanism of SnO₂-DNTs

After determining the composition and structural characteristics of SnO₂-DNTs, we try to understand its growth mechanism by studying the morphological evolution from ZnO NRs to SnO₂-DNTs. Taking the precursor concentration of 6 mM as an example, TEM images of the samples grown at different periods during the hydrothermal synthesis are shown in Fig. 4. As depicted in Fig. 4 (a), when the reaction time is 15 min, the sample exhibits the

ZnO/SnO₂ core/shell nanorod structure with a porous SnO₂ shell of about 20 nm thick wrapping the surface of the ZnO NRs. At this time, the ZnO NRs cores retain its rod-shaped structure as marked by red circle. As the reaction time increases to 30 min, the core templates begin to be partially etched off as shown in Fig. 4(b), but some incomplete ZnO NRs core still remain. Moreover, the ZnO NRs are smashed into numerous tiny patches, indicating an *in situ* self-etching process. Meanwhile, the nanotube shell thickness increases to 30 nm at this reaction stage. With prolonging the reaction time to 60 min, the tubular structure with a thicker wall is already formed completely as shown in Fig. 4(c), which implies that almost all the ZnO NRs are etched off. Intriguingly, the resulting nanotube is covered with a dome-like cap on one tip, which is in good agreement with SEM observation. Finally, if the reaction time prolongs to 90 min, the SnO₂ shells become thick enough to fill the nanotube. Therefore, in order to grow the SnO₂-DNTs by this *in situ* SE strategy, the reaction time should be appropriate controlled, and the shell thickness can be tuned. The influence from the sodium stannate precursor concentration are also investigated by fixing the reaction time at 60 min, and the corresponding TEM images of the SnO₂-DNTs are shown in Fig. S4. In our case, the optimized reaction time is 60 min for 6 mM sodium stannate. Under this condition, the SnO₂-DNTs array with well-defined structure and proper diameter is obtained.

Based on the above discussion, the chemical formation process of SnO₂-DNTs was proposed as illustrated in Fig. 5. Firstly, the ZnO NRs are synthesized on FTO glass substrate, and then during the hydrothermal growth process, the deposition of SnO₂ shell and

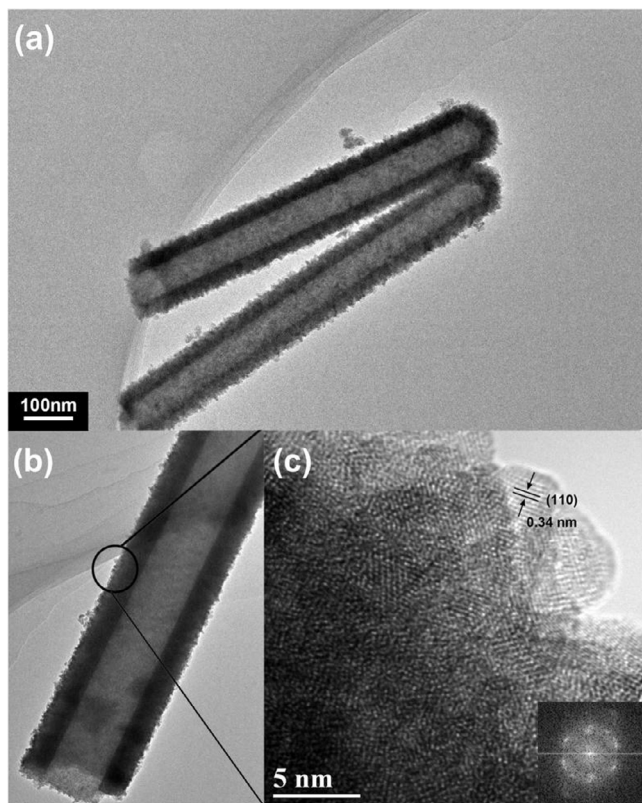


Fig. 2. Low magnification TEM images (a, b) and high-resolution TEM image (c) of SnO₂-DNTs. The inset shows typical FFT pattern of (b).

the etching of ZnO NRs template proceed at the same time. The formation of SnO₂ derives from the interactions of sodium stannate and urea. With the increase of temperature, urea starts to hydrolyze, generating carbon dioxide (CO₂) and ammonia (NH₃) via $\text{CO}(\text{NH}_2)_2 + \text{H}_2\text{O} \rightarrow \text{CO}_2 + \text{NH}_3$. Simultaneously, sodium stannate could gradually react with CO₂, and produce SnO₂ crystallites via $\text{Na}_2\text{SnO}_3 + \text{CO}_2 \rightarrow \text{SnO}_2 + \text{Na}_2\text{CO}_3$ [19]. Besides that, with the hydrolysis of urea under hydrothermal conditions, an alkaline solution is formed via $\text{NH}_3 + \text{H}_2\text{O} \rightarrow \text{NH}_4^+ + \text{OH}^-$, which provides the chemical dynamics to form the hollow tube-shaped structure. As ZnO is a typical amphoteric oxide, ZnO NRs could be *in situ* dissolved by the self-generated OH⁻. Essentially, the consumption of OH⁻ by ZnO NRs could accelerate the hydrolysis of urea, in turn, leading to produce more CO₂, which induces more sodium stannate consumed and promotes the synthesis of SnO₂ shell onto the ZnO NRs. With the reaction continuing, more OH⁻ is generated and ZnO NRs are gradually etched off [38]. Importantly, it should be mentioned that the initial ZnO seed layer modified onto the surface of FTO substrate through pulsed laser deposition method is partly preserved after the transformation to SnO₂-DNTs [39], as shown in Fig. S5, which is essential for the perovskite solar cell application as an electron transport layer should be maintained.

3.3. SnO₂-DNTs as effective ETL for perovskite solar cell

Although ZnO film and nanostructures are reported to be a good ETL candidate for perovskite solar cell, the thermal stability of ZnO/perovskite interface is still a problem [40]. To further confirm its application in perovskite solar cell, we first check the thermal stability of the SnO₂-DNTs/perovskite interface. Namely, CH₃NH₃PbI₃ perovskite films were spin coated onto the SnO₂-DNTs that was synthesized under different reaction time. Then those bilayers were annealed for 10 min, 30 min and 60 min, respectively. Fig. 6 (a) presents the optical images of SnO₂-DNTs/perovskite bilayer

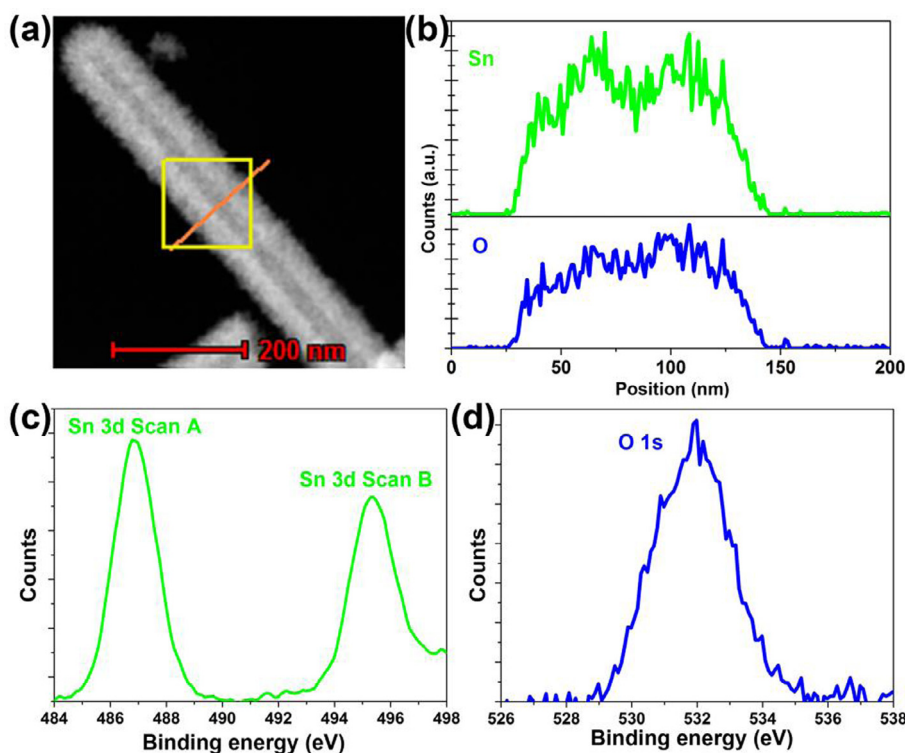


Fig. 3. (a) Dark field TEM image of a single tubular SnO₂ structure (b) compositional line scanning profile along the orange line indicated in (a); (c) and (d) are the high-resolution XPS spectra for Sn.

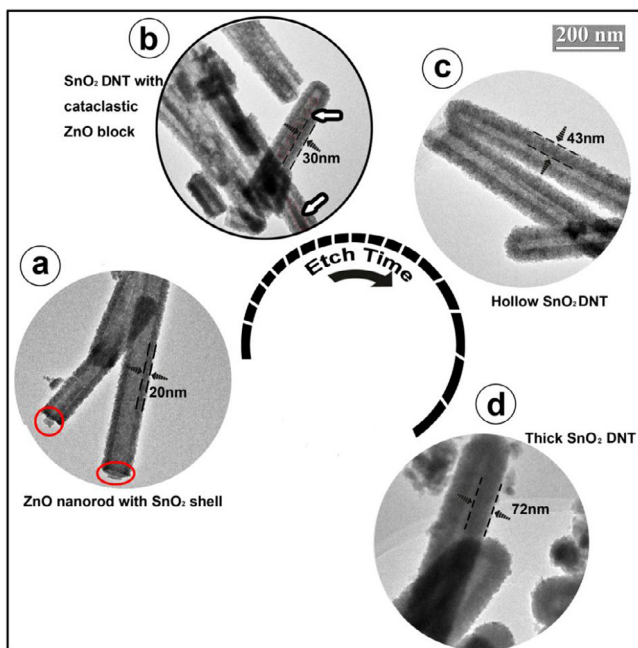


Fig. 4. Time-dependent growth process of SnO_2 -DNTs. Typical TEM images of the SnO_2 -DNTs grown under the different reaction time: (a) 15 min, (b) 30 min, (c) 60 min, (d) 90 min.

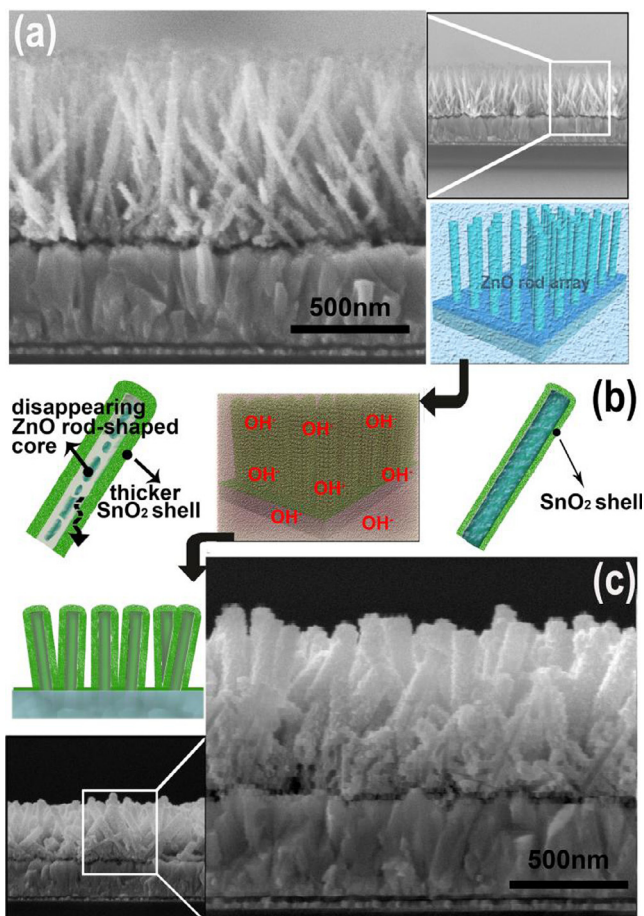


Fig. 5. Chemical illustration of the growth mechanism for SnO_2 -DNTs. (a) ZnO NRs covered with a thin and discontinuous SnO_2 nanoparticle layer; (b) the OH^- ions as the by-product of SnO_2 can etch the ZnO NRs off; (c) SnO_2 -DNTs with preserved ZnO NRs array morphology on substrate.

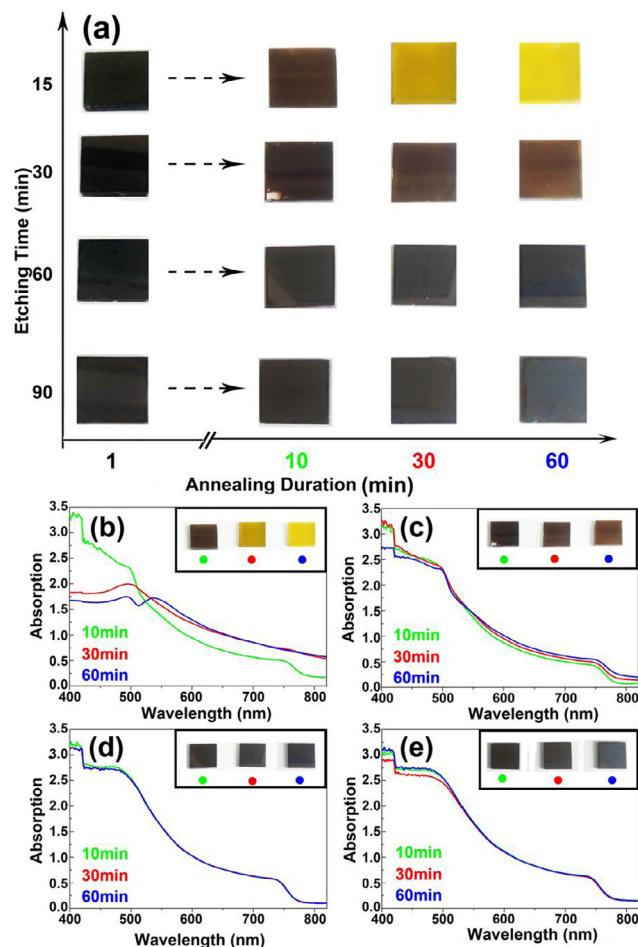


Fig. 6. (a) Perovskite films were spin-coated on SnO_2 -DNTs grown on FTO/glass substrate and annealed at 100°C in glove box for different time (X-axis). Y-axis indicates the growth time of SnO_2 -DNTs including 15 min, 30 min, 60 min, and 90 min. Black color means the perovskite/ SnO_2 interface is stable while the yellow color (PbI_2) means the perovskite decomposition. (b–e) show absorption spectra of the perovskite/ SnO_2 -DNTs bilayers in (a). Insets are the corresponding optical images.

annealed at different time and Fig. 6(b–e) and Fig. S6 are the corresponding absorption spectra and XRD patterns. Obviously, the degraded perovskite film with a certain amount of PbI_2 is observed for SnO_2 partially coated ZnO NRs if the growth time is short, e.g. 15 min or 30 min. With the gradual formation of SnO_2 -DNTs, the thermal stability of perovskite film on ZnO/ SnO_2 nanostructure is improved, which derives from the depletion of ZnO NRs template. Particularly, since ZnO NRs templates are completely exhausted for the 60 min and 90 min samples, the perovskite/ SnO_2 shows a superior thermal stability and phase purity, indicating a good device performance can be expected.

After confirming the growth controllability of such SnO_2 nanostructure and thermal stability of perovskite/ SnO_2 interface, we fabricated perovskite solar cells with a configuration of glass/FTO/ SnO_2 -DNTs/perovskite/P3HT/Au, as displayed in Fig. 7(a), where the SnO_2 -DNTs with optimized morphology are used as ETL. The cross sectional SEM image of the device is shown in Fig. 7(b), and such SnO_2 -DNTs array is fully filled with dense perovskite film, on top of which P3HT as HTL and Au electrode are further deposited.

In Fig. 7(c–d), we plot the current density-voltage (J–V) curves and the corresponding external quantum efficiency (EQE) of the best performance, where the SnO_2 -DNTs were grown by of the above iTSE strategy. The J–V characteristic delivers a short-circuit

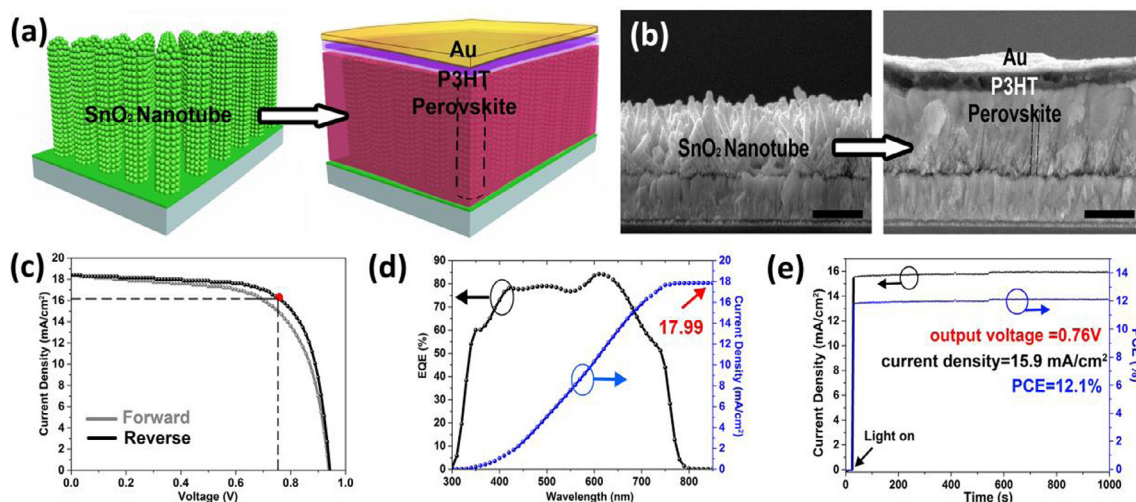


Fig. 7. (a) Scheme of fabrication process of perovskite solar cell; (b) the corresponding cross-sectional SEM images of SnO₂-DNTs and SnO₂-DNTs/perovskite/P3HT/Au devices. The scale bar is 500 nm; (c) I-V curves of the best SnO₂-DNTs/perovskite/P3HT/Au device with different scanning directions (forward and reverse); (d) The corresponding EQE spectrum and integrated current density; (e) Stable photocurrent and PCE output performance, where the bias voltage is fixed at 0.76 V. All of these measurements were carried out under ambient atmosphere with relative humidity about 30%.

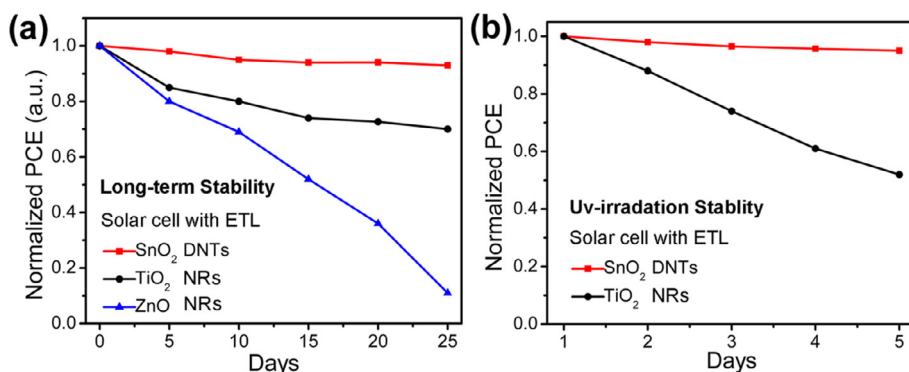


Fig. 8. (a) Long-term stability of SnO₂-DNTs (red curve), TiO₂-NRs (black curve), and ZnO-NRs (blue curve) based perovskite solar cells; (b) UV-stability comparison of SnO₂-DNTs (red curve) and TiO₂ based (black curve) perovskite solar cells. (For interpretation of the references to colour in this figure legend, the reader is referred to the web version of this article.)

current density (J_{sc}) of 18.38 mA/cm², an open-circuit voltage (V_{oc}) of 0.94 V and a fill factor (FF) of 70.7%, which gives a PCE of 12.26% for reverse scanning ($V_{oc} \rightarrow J_{sc}$). Meanwhile, the forward scanning exhibits a J_{sc} of 18.44 mA/cm², a V_{oc} of 0.94 V, and a FF of 65% achieving a PCE of 11.3%, which shows a relatively weak hysteresis phenomenon [41].

The integrated current density extracted from the corresponding EQE curve (Fig. 7(d)) gives a value of 17.99 mA/cm², which is very comparable with the J-V scanning curves. In addition, to further confirm the device stability and output property, the steady-state photocurrent output at the maximum power point as indicated with red dot is measured as shown in Fig. 7(c). The steady-state photocurrent represents the real power output and should be used to accurately characterize the device efficiency. As shown in Fig. 7(e), the steady-state current can fix at 15.9 mA/cm² with a stable PCE of 12.1% for a long duration over 1000 s. These device performances demonstrate that such SnO₂-DNTs possess a superior carrier transporting property and a proper energy level matching with perovskite. It should be noted that, compared with the generally adopted hole transport material Spiro-OMeTAD, we select pure P3HT in this work, which has a better chemical stability [42–45]. Without doping of Li-TFSI and the oxidation procedure, it suppresses the decomposition of perovskite

film. Considering adopting the P3HT as HTM, this device with stable output efficiency over 12% presents a high photovoltaic performance [46].

Device performance distributions for a batch of 14 devices measured under AM 1.5 simulated solar irradiation are shown in Fig. S7. The voltage was scanned from V_{oc} to J_{sc} at a scan rate of 0.3 V/s. The average J_{sc} , V_{oc} , and FF achieves a value of 17.9 mA/cm², 0.93 V, and 68 %, respectively, and the average PCE are calculated as over 10%. Devices performances provide direct evidence that such novel SnO₂-DNTs possess effective electron transporting nature for perovskite solar cell application. One main reason is that the well-matched crystalline interface between SnO₂ nanotube and FTO substrate will minimize defects at this internal surface, enabling ease of electron transfer from the perovskite to the SnO₂ and also avoid any extra internal trap sites, which would otherwise be present in a heterojunction like ZnO/FTO ETL. In addition, the impedance spectrum of a solar cell device based on the structure of SnO₂-DNTs/perovskite P3HT/Au was measured under light (0.5 sun) with 1V bias, as shown in Fig. S8.

Recently, the long-term stability and UV-stability of PSCs has obtained much attention because PSCs must be able to withstand these conditions for their commercialization. In this work, the comparison of long-term and UV-stability of SnO₂-DNTs based

perovskite solar cell with traditional TiO₂ and ZnO PSCs have been carried out. Fig. 8(a) compares the normalized PCE of SnO₂, TiO₂ NRs, and ZnO NRs ETL based perovskite solar cells in 25 days, while Fig. 8(b) shows the normalized PCEs of the unencapsulated SnO₂ cell and TiO₂ cell in a nitrogen-filled glove box with constant 267 nm UV lamp illumination. No matter in terms of long-term stability or UV-stability, the PSC with SnO₂-DNTs as ETL is much better than the device with TiO₂ or ZnO ETL.

4. Conclusions

In this work, we synthesized the novel hollow domed SnO₂ nanotubes (SnO₂-DNTs) utilizing the *in situ* self-etching template strategy and demonstrated their successful application as effective and stable ETL for perovskite solar cell. ZnO NRs template could be etched off along with the formation of SnO₂ shell, and the hydrolysis of urea plays a critical role during the preparation process, which provides CO₂ and NH₃. The former reacts with sodium stannate and produces SnO₂ crystallites, and the latter induces an alkaline chemical surrounding to etch the ZnO template off. Perovskite solar cells based on the novel SnO₂-DNTs were fabricated for the first time. With the structure of FTO/SnO₂-DNTs/perovskite/P3HT/Au, the best device presents a stable PCE of 12.1%, confirming the great electrons transporting property of the SnO₂-DNTs. Moreover, the PSC with SnO₂-DNTs as ETL exhibits better long-term stability and UV-stability than similar TiO₂ or ZnO PSCs. We suggest that the SnO₂-DNTs array can be employed in many fields including field emission devices, lithium ion battery, and high-performance gas sensors.

Notes

The authors declare no competing financial interest.

Acknowledgements

BQ is supported by NSFC (51472110), and Shandong Provincial Natural Science Foundation (2014ZR01A47). BQ also thanks the Taishan Scholar Chaired Professorship tenured at University of Jinan. JH is supported by NSFC (21475052, 21277058).

Appendix A. Supplementary data

Supplementary data associated with this article can be found, in the online version, at <http://dx.doi.org/10.1016/j.cej.2017.05.085>.

References

- [1] A. Kojima, K. Teshima, Y. Shirai, T. Miyasaka, *J. Am. Chem. Soc.* 131 (2009) 6050–6051.
- [2] H. Choi, J.H. Heo, S. Ha, B.W. Kwon, S.P. Yoon, J. Han, W. Kim, S.H. Im, J. Kim, *Chem. Eng. J.* 310 (2017) 179–186.
- [3] Z.M. Zhou, Z.W. Wang, Y.Y. Zhou, S.P. Pang, D. Wang, H.X. Xu, Z.H. Liu, N.P. Padture, G.L. Cui, *Angew. Chem. Int. Ed.* 54 (2015) 9705–9709.
- [4] M.Z. Liu, M.B. Johnston, H.J. Snaith, *Nature* 501 (2013) 395–398.
- [5] D.Q. Bia, B. Xub, P. Gaod, L.C. Sunb, M. Grätzele, A. Hagfeldt, *Nano Energy* 23 (2016) 138–144.
- [6] W.Z. Fan, J.D. Li, J.W. Li, Y.H. Mai, L.D. Wang, *J. Am. Chem. Soc.* 137 (2015) 10399–10405.
- [7] J.H. Im, C.R. Lee, J.W. Lee, S.W. Parka, N.G. Park, *Nanoscale* 3 (2011) 4088–4093.
- [8] G.F. Hu, W.X. Guo, R.M. Yu, X.N. Yang, R.R. Zhou, C.F. Pan, Z.L. Wang, *Nano Energy* 23 (2016) 27–33.
- [9] D.Y. Son, K.H. Bae, H.S. Kim, N.G. Park, *J. Phys. Chem. C* 119 (2015) 10321–10328.
- [10] D.Y. Son, J.H. Im, H.S. Kim, N.G. Park, *J. Phys. Chem. C* 118 (2014) 16567–16573.
- [11] M. Chen, R.H. Zha, Z.Y. Yuan, Q.S. Jing, Z.Y. Huang, X.K. Yang, S.M. Yang, X.H. Zhao, D.L. Xu, G.D. Zou, *Chem. Eng. J.* 313 (2017) 791–800.
- [12] H.S. Kim, C.R. Lee, J.H. Im, K.B. Lee, T. Moehl, A. Marchioro, S.J. Moon, R.H. Baker, J.H. Yum, J.E. Moser, M. Grätzel, N.G. Park, *Sci. Rep.* 2 (2012) 591.
- [13] X.X. Huang, H.K. Wang, C.M. Niu, A.L. Rogach, *CrystEngComm* 17 (2015) 5593–5604.
- [14] C.Y. Huang, W.F. Fu, C.Z. Li, Z.Q. Zhang, W.M. Qiu, M.M. Shi, P. Heremans, A.K.Y. Jen, H.Z. Chen, *J. Am. Chem. Soc.* 138 (2016) 2528–2531.
- [15] T. Leijtens, G.E. Eperon, N.K. Noel, S.N. Habisreutinger, A. Petrozza, H.J. Snaith, *Adv. Energy Mater.* 5 (2015) 1500963.
- [16] Y.H. Cheng, Q.D. Yang, J.Y. Xiao, Q.F. Xue, H.W. Li, Z.Q. Guan, H.L. Yip, S.W. Tsang, *ACS Appl. Mater. Interfaces* 7 (2015) 19986–19993.
- [17] X.Y. Zhao, H.P. Shen, Y. Zhang, X. Li, X.C. Zhao, M.Q. Tai, J.F. Li, J.B. Li, X. Li, H. Lin, *ACS Appl. Mater. Interfaces* 8 (2016) 7826–7833.
- [18] L.J. Zuo, Z.W. Gu, T. Ye, W.F. Fu, G. Wu, H.Y. Li, H.Z. Chen, *ACS Appl. Mater. Interfaces* 137 (2015) 2674–2679.
- [19] V. Juttukonda, R.L. Paddock, J.E. Raymond, D. Denomme, A.E. Richardson, L.E. Slusher, B.D. Fahlman, *J. Am. Chem. Soc.* 128 (2006) 420–421.
- [20] D.F. Zhang, L.D. Sun, C.J. Jia, Z.G. Yan, L.P. You, C.H. Yan, *J. Am. Chem. Soc.* 127 (2005) 13492–13493.
- [21] H.T. Ng, J. Li, M.K. Smith, P. Nguyen, A. Han, J. Cassell, M. Meyyappan, *Science* 300 (2003) 1249.
- [22] T. Leijtens, G.E. Eperon, S. Pathak, A. Abate, M.M. Lee, H.J. Snaith, *Nat. Commun.* 4 (2013) 2885.
- [23] P. Tiwana, P. Docampo, M.B. Johnston, H.J. Snaith, L.M. Herz, *ACS Nano* 5 (2011) 5158–5166.
- [24] G.S. Han, H.S. Chung, D.H. Kim, B.J. Kim, J.W. Lee, N.G. Park, I.S. Cho, J.K. Lee, S. Lee, H.S. Jung, *Nanoscale* 7 (2015) 15284–15290.
- [25] B. Bob, T.B. Song, C.C. Chen, Z. Xu, Y. Yang, *Chem. Mater.* 25 (2013) 4725–4730.
- [26] W.J. Ke, G.J. Fang, Q. Liu, L.B. Xiong, P.L. Qin, H. Tao, J. Wang, H.W. Lei, B.R. Li, J. W. Wan, G. Yang, Y.F. Yan, *J. Am. Chem. Soc.* 137 (2015) 6730–6733.
- [27] L.B. Xiong, M.C. Qin, G. Yang, Y.X. Guo, H.W. Lei, Q. Liu, W.J. Ke, H. Tao, P.L. Qin, S.Z. Li, H.Q. Yu, G.J. Fang, *J. Mater. Chem. A* 4 (2016) 8374–8383.
- [28] H.J. Snaith, C. Ducati, *Nano Lett.* 10 (2010) 1259–1265.
- [29] S. Gubbala, V. Chakrapani, V. Kumar, M.K. Sunkara, *Adv. Funct. Mater.* 18 (2008) 2411.
- [30] Y.L. Wang, M. Guo, M. Zhang, X.D. Wang, *CrystEngComm* 12 (2010) 4024–4027.
- [31] G. Murugadoss, H. Kanda, S. Tanaka, H. Nishino, S. Ito, H. Imahori, T. Uemeyama, *J. Power Sour.* 307 (2016) 891–897.
- [32] Q. Kuang, T. Xu, Z.X. Xie, S.C. Lin, R.B. Huang, L.S. Zheng, *J. Mater. Chem.* 19 (2009) 1019–1023.
- [33] J.Z. Wang, N. Du, H. Zhang, J.X. Yu, D.R. Yang, *J. Phys. Chem. C* 115 (2011) 11302–11305.
- [34] X.F. Qiu, L. Chen, H.B. Gong, M. Zhu, M. Zi, X.P. Yang, C.J. Ji, B.Q. Cao, *J. Colloids Interface. Sci.* 430 (2014) 200–206.
- [35] C.M. Gao, L.N. Zhang, Y.H. Wang, J.H. Yu, X.R. Song, *Biosens. Bioelectron.* 83 (2016) 327–333.
- [36] J.F. Moulder, W.F. Sticke, K.P.E. Sobol, D. Bomben, in *Handbook of X-ray photoelectron spectroscopy* J. Chastain, R.C. King, Jr., Eds. Perkin-Elmer Corp: Eden Prairie, MN, 1995, p 127.
- [37] A.R. Babar, S.S. Shinde, A.V. Moholkar, K.Y. Rajpure, *J. Alloys Compd.* 6 (2011) 3108–3115.
- [38] G.W. She, X.H. Zhang, W.S. Shi, X. Fan, J.C. Chang, C.S. Lee, S.T. Lee, C.H. Li, *Appl. Phys. Lett.* 92 (2008) 053111.
- [39] Y.F. Tu, Q.M. Fu, X.J. Niu, J.P. Sang, Z.J. Tan, X.W. Zou, *J. Mater. Sci. Technol.* 29 (2013) 1053–1058.
- [40] J.L. Yang, B.D. Siempelkamp, E. Mosconi, F.D. Angelis, T.L. Kelly, *Chem. Mater.* 27 (2015) 4229–4236.
- [41] H.S. Kim, I.H. Jiang, N. Ahn, M. Choi, A. Guerrero, J. Bisquert, N.G. Park, *J. Phys. Chem. Lett.* 6 (2015) 4633–4639.
- [42] J. Liu, Y.Z. Wu, C.J. Qin, X.D. Yang, T. Yasuda, A. Islam, K. Zhang, W.Q. Peng, W. Chen, L.Y. Han, *Energy Environ. Sci.* 7 (2014) 2963–2967.
- [43] J. Ye, X.L. Li, J.J. Zhao, X.L. Mei, Q. Li, *RSC Adv.* 6 (2016) 36356–36361.
- [44] J.Y. Xiao, J.J. Shi, H.B. Liu, Y.Z. Xu, S.T. Lv, Y.H. Luo, D.M. Li, Q.B. Meng, Y.L. Li, *Adv. Energy Mater.* 5 (2015) 1401943.
- [45] Q.Q. Zhu, X.C. Bao, J.H. Yu, D.Q. Zhu, M. Qiu, R.Q. Yang, L.F. Dong, *ACS Appl. Mater. Interfaces* 8 (2016) 2652–2657.
- [46] D.Y. Liu, T.L. Kelly, *Nat. Photon.* 8 (2014) 133–138.